

This work was written as part of one of the author's official duties as an Employee of the United States Government and is therefore a work of the United States Government. In accordance with 17 U.S.C. 105, no copyright protection is available for such works under U.S. Law.

Public Domain Mark 1.0

<https://creativecommons.org/publicdomain/mark/1.0/>

Access to this work was provided by the University of Maryland, Baltimore County (UMBC) ScholarWorks@UMBC digital repository on the Maryland Shared Open Access (MD-SOAR) platform.

Please provide feedback

Please support the ScholarWorks@UMBC repository by emailing scholarworks-group@umbc.edu and telling us what having access to this work means to you and why it's important to you. Thank you.

ENSO Disrupts Boreal Winter CRE Feedback

DAEHO JIN^{a,b}, RYAN J. KRAMER^{a,b}, LAZAROS OREOPOULOS^b, AND DONGMIN LEE^{c,b}

^a *GESTAR-II, University of Maryland, Baltimore County, Baltimore, Maryland*

^b *Earth Sciences Division, NASA's Goddard Space Flight Center, Greenbelt, Maryland*

^c *GESTAR-II, Morgan State University, Baltimore, Maryland*

(Manuscript received 11 May 2023, in final form 27 October 2023, accepted 31 October 2023)

ABSTRACT: Twenty years of satellite-based cloud and radiation observations allow us to examine the observed cloud radiative effect (CRE) feedback (i.e., CRE change per unit change in global mean surface temperature). By employing a decomposition method to separate the contribution of “internal changes” and “relative-frequency-of-occurrence (RFO) changes” of distinct cloud regime (CR) groups, notable seasonal contrasts of CRE feedback characteristics emerge. Boreal winter CRE feedback is dominated by the positive shortwave CRE (SWCRE) feedback of oceanic low-thick clouds, due to their decreasing RFO as temperature rises. This signal is most likely due to El Niño–Southern Oscillation (ENSO) activity. When ENSO signals are excluded, boreal winter CRE feedback becomes qualitatively similar to the boreal summer feedback, where several CR groups contribute to the total CRE feedback more evenly. Most CR groups' CRE feedbacks largely come from changing RFO (e.g., the predominant transition from oceanic cumulus to broken clouds and more occurrences of higher convective clouds with warming temperature). At the same time, low-thick and broken clouds experience optical thinning and decreasing cloud fraction, and these features are more prominent in boreal summer than winter. Overall, the seasonally asymmetric patterns of CRE feedback, primarily due to ENSO, introduce complexity in assessments of CRE feedback.

KEYWORDS: Cloud radiative effects; ENSO; Seasonal effects; Climate change; Feedback; Satellite observations

1. Introduction

Despite the importance of reliable global warming assessments, even the most sophisticated global climate models (GCMs) exhibit large uncertainties in simulating climate change. This is mainly due to the complex interactions among various components of Earth's climate system such as clouds, water vapor, snow/ice albedo, and biogeochemistry (Forster et al. 2021). Among these factors, clouds and their radiative influence on Earth's energy balance is the largest source of uncertainty in warming projections (e.g., Kamae et al. 2016; Soden and Held 2006; Zelinka et al. 2020).

Cloud feedbacks, namely the radiative response to global warming-induced cloud changes, are typically examined using numerical model experiments. For example, in the pioneering work by Wetherald and Manabe (1988), a set of experiments was used to assess the change of radiative fluxes in response to perturbations of specific variables. Later, Cess et al. (1990, 1996) performed experiments with perturbed sea surface temperatures (SSTs) and examined the role of clouds in radiative flux changes using the concept of cloud radiative effect (CRE), the difference between all-sky (including clouds) and clear-sky

(cloudless) fluxes. However, it has become widely accepted that such a CRE-based calculation is not the most accurate assessment of the narrowly defined cloud feedback, since it also includes the cloud masking of noncloud changes, which is not considered as cloud feedback per se (e.g., Zhang et al. 1994; Colman 2003; Soden et al. 2004), as well as changes in clear-sky fluxes. These confounding factors, and the nonlinearity of cloud feedback, demand more sophisticated analyses such as those that can be achieved with the “radiative kernel” (Soden et al. 2008) and partial radiative perturbation (PRP) methods (Colman and McAvaney 1997; Wetherald and Manabe 1988). Radiative kernels have been used in GCMs to diagnose uncertainty in global-mean radiative forcing and feedbacks relevant for climate sensitivity (e.g., Smith et al. 2020; Soden et al. 2008) and the hydrological cycle (Myhre et al. 2018; O’Gorman et al. 2012), and also to understand the role of radiative changes in physical processes such as convective organization (Bony et al. 2020; Zhang et al. 2019).

To diagnose specifically cloud feedback, the concept of the “cloud radiative kernel (CRK)” was developed to capture the radiative effects of clouds whose populations are distributed in 2D joint histograms of cloud-top pressure (CTP) and optical thickness (COT) (Zelinka et al. 2012a,b, 2016). Such histograms are prominently featured in International Satellite Cloud Climatology Project (ISCCP) observations (Rossow and Schiffer 1991, 1999) and their GCM simulators (Bodas-Salcedo et al. 2011; Klein and Jakob 1999; Webb et al. 2001). The CRK framework has advanced our understanding of what kind of cloud changes contribute to feedbacks. Recently Zelinka et al. (2023, hereinafter Z23) reported further details of cloud feedbacks in GCMs by combining CRKs with model clouds assigned to ISCCP cloud regimes (Jakob and Tselioudis 2003; Rossow et al. 2005; Tselioudis

Supplemental information related to this paper is available at the Journals Online website: <https://doi.org/10.1175/JCLI-D-23-0282.s1>.

Kramer's current affiliation: Geophysical Fluid Dynamics Laboratory, NOAA, Princeton, New Jersey

Corresponding author: Daeho Jin, daeho.jin@nasa.gov

DOI: 10.1175/JCLI-D-23-0282.1

© 2023 American Meteorological Society. This published article is licensed under the terms of the default AMS reuse license. For information regarding reuse of this content and general copyright information, consult the AMS Copyright Policy (www.ametsoc.org/PUBSReuseLicenses).

Brought to you by UNIVERSITY OF MD BALTIMORE COUNTY | Unauthenticated | Downloaded 05/07/24 04:55 PM UTC

et al. 2013, 2021). Z23 analyzed inter- and intra-regime responses to increased surface temperature, and found models to consistently simulate decreases of cloud amount and increases of cloud albedo with warming, and a thinning (thickening) of tropical (extratropical) clouds.

Observations from the Moderate Resolution Imaging Spectroradiometer (MODIS) and Clouds and the Earth's Radiant Energy System (CERES) sensors aboard the *Terra* and *Aqua* satellites are now available for more than 20 years, sufficient for examining trends in Earth's energy budget and role of cloud feedback. For example, Loeb et al. (2021) showed a notable positive trend of Earth's energy imbalance based on satellite observations, while Raghuraman et al. (2023) examined the offsetting effect of opposing longwave CRE (LWCRE) and shortwave CRE (SWCRE) trends contributing to near-zero trend of net CRE. In this study we examine the decomposition of cloud feedbacks by cloud regimes following Z23, but based solely on MODIS and CERES observations and without invoking CRs. The objective is to examine cloud-related radiation changes contemporaneous with mean surface temperature change (i.e., CRE feedback), by applying Z23's concept of decomposing CRE changes to those due to within-regime cloud property changes and regime occurrence changes. Feedback characteristics are contrasted not only between land and ocean, but also between seasons, the latter examined to test the hypothesis that dramatically different seasonal distribution of clouds respond differently to global warming. Notably, the El Niño–Southern Oscillation (ENSO) activity strongly affecting global climate at interannual time scales is asymmetrically strong in boreal winter compared to boreal summer, thus necessitating a seasonal CRE feedback analysis.

2. Data and cloud regimes

a. Radiation flux and surface temperature

Radiative fluxes at the top of the atmosphere (TOA) are obtained from the CERES Flux by Cloud Type (FBCT) product, which is available daily at 1° resolution (Sun et al. 2022) and provides exact spatiotemporal matching with MODIS cloud regimes since it is based on MODIS radiances. The FBCT product comprises only daytime fluxes since it resolves fluxes in the COT-CTP phase space and COT is retrievable only during daytime. Clear-sky FBCT fluxes are missing for about 20% of grid cells on average due to either unavailable satellite observations or overcast conditions. We filled this missing data via linear interpolation in space and time. When we tested one of our key results with the more complete CERES Energy Balance and Filled (EBAF) monthly data (Loeb et al. 2018), we confirmed that our gap-filled FBCT data are reliable (see section 3a).

The global surface temperature comes from MERRA-2 [surface skin temperature (T_s); Gelaro et al. 2017]. We focus on 3-month means [December–February (DJF) and June–August (JJA); i.e., seasonal means] for the period of December 2002–August 2022 (20 seasons), in the “near-global” domain of 60°S–60°N. Area-weighted domain mean values are well approximated by using cosine of latitude weights. When comparing the results based on MERRA-2 T_s with those based on the

Hadley Centre sea ice and sea surface temperature (SST) dataset (HadISST; Rayner et al. 2003), we find the CRE feedback magnitudes generally larger for the latter, since SST variability is smaller than that of T_s , but conclusions are not affected. The p value for regression analysis is calculated according to the effective degrees of freedom derived from auto- and cross-correlations (Afyouni et al. 2019).

b. Cloud regimes

The cloud classification is based on cloud regimes (CRs), obtained via k -means clustering of MODIS 2D joint histograms of COT and CTP (Collection 6.1; Platnick et al. 2017, 2018), and shown to be useful in various studies (e.g., Jin et al. 2022, 2023, Tselioudis et al. 2021). While the clustering process used distinct *Terra* and *Aqua* joint histograms in the 50°S–50°N domain (at daily 1° resolution from June 2014 to May 2019; Jin et al. 2021), regime assignment for a particular grid cell was performed using the average *Terra*–*Aqua* joint histogram (TA_mean) in the extended 60°S–60°N domain from September 2002 to August 2022. This approach minimizes unassigned grid cells and ensures that the cloud classification represents daytime mean observations while utilizing the most available cloud observations. Details about the CRs are presented in the appendix.

The full set of 17 CRs (including the subregimes) capture in great detail the characteristics of global cloudiness. However, for studying CRE feedback, this large number of CRs makes the analysis, interpretation of results, and presentation somewhat cumbersome. Hence, we proceeded to organize the CRs into eight groups: tropical high thick (H1_tk) and thin (H1_tn) clouds, and lower-altitude high clouds that are mostly extratropical and were also divided into thick (H2_tk) and thin (H2_tn), midlevel clouds (Mid), thick (L_tk) and thin (L_tn) low clouds, and semiclear clouds (S-Clr). The grid cells for which no CR was assigned (e.g., completely clear sky or missing in the MODIS dataset) are designated as “CS+Ms”. The combined joint histogram of CR centroids and mean RFO map of CRs assigned to each group are shown in Fig. 1. CR members for each group and seasonal mean RFOs of the CR groups by land/ocean are provided in Table 1, indicating that seasonal differences in terms of mean RFO are small. The seasonal mean properties of SWCRE and LWCRE are similar for the CRs within each group (Fig. S1 in the online supplemental material), affirming that the CR groups can serve as a representative summary of the individual CR behaviors. This figure shows that the largest absolute values of SWCRE/LWCRE correspond to H1_tk clouds, although the CRE contribution is dominated by S-Clr clouds because their RFO (about 40%) dwarfs those of all other CR groups (not shown).

3. CRE feedbacks and their decomposition

a. Seasonal mean CRE feedback

In this study CRE feedback α is defined as in previous studies (e.g., Chung and Soden 2018), with the CRE (X) and domain mean surface temperature (T_s):

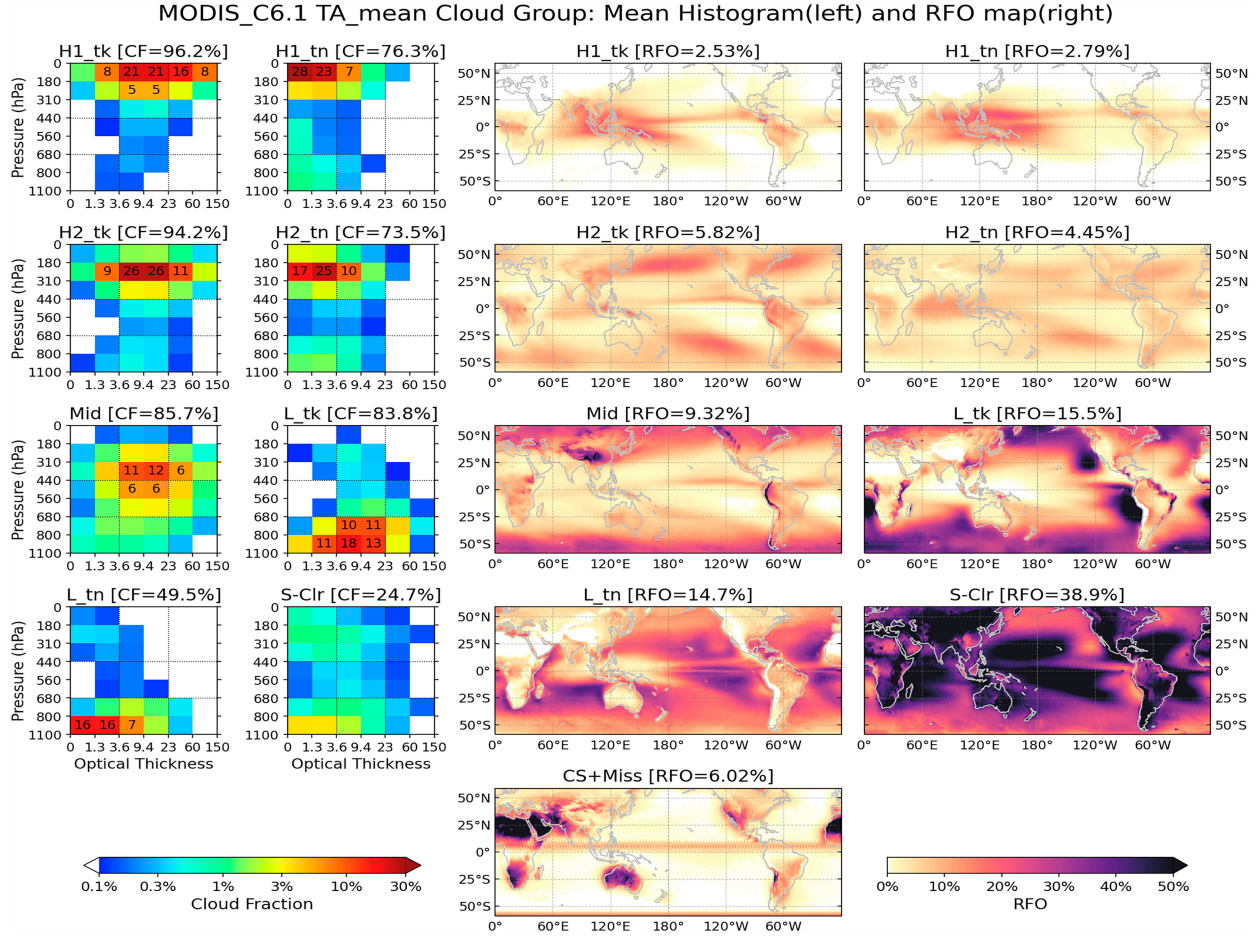


FIG. 1. (left) CR group mean joint histograms and (right) geographical distribution of relative frequency of occurrence (RFO) after *Terra-Aqua* mean (TA_mean) histograms were assigned into 60°S–60°N domain (September 2002–August 2022). The mean RFO provided above each map panel is obtained by using a cosine of latitude weight when averaging the RFO distribution (for consistency to temperature and radiation variables), and mean joint histograms are obtained from weighted average by mean RFO of each CR. Bin cloud fraction values exceeding 5% are shown explicitly on the joint histograms, with the total cloud fraction of each CR group also shown above each joint histogram.

$$\alpha = \frac{\partial X}{\partial T_s}. \quad (1)$$

The value of α can be obtained by a linear regression of X against T_s .

$$X = \alpha T_s + \beta + \epsilon, \quad (2)$$

where β is the intercept, and ϵ is the residual

For this analysis, the β term is irrelevant and is ignored. Figure 2 shows the 20-yr distribution of seasonal and near-global mean SWCRE/LWCRE versus T_s , and corresponding linear regression lines for DJF and JJA. The variability of T_s is larger in DJF than JJA, while that of SWCRE is similar in the two seasons, thus resulting in larger SWCRE feedback (= steeper slope of regression line) in JJA ($2.31 \text{ W m}^{-2} \text{ K}^{-1}$) than DJF ($1.73 \text{ W m}^{-2} \text{ K}^{-1}$). The regression slope of LWCRE is also steeper in JJA than DJF (-1.36 vs $-0.54 \text{ W m}^{-2} \text{ K}^{-1}$).

Positive SWCRE feedback means less outgoing SW radiation (less reflection) as surface warms, and negative LWCRE feedback means more outgoing LW radiation with warming, thus competing against each other. The correlations between CRE and T_s , are fairly strong (coefficient magnitudes > 0.57) with low p values (< 0.053) indicating that the relationships are significant with high confidence except for LWCRE in DJF ($r = -0.273$; insignificant at the 90% confidence level). When comparing SWCRE and LWCRE, SWCRE is more strongly correlated with DJF T_s , while LWCRE is more strongly correlated with JJA T_s . We also repeated this analysis for both seasons with CERES EBAF monthly data (Ed. 4.2; Fig. S2) and confirmed their consistency with these FBCT results. We find these seasonal differences of SWCRE/LWCRE feedback signals to be mainly driven by El Niño–Southern Oscillation (ENSO), which is more active in DJF (see section 4a). It is worth noting that the global warming trend in terms of T_s is more notable in

TABLE 1. Area-weighted relative frequency of occurrence (RFO) within 60°S–60°N for our cloud regime (CR) groups and the group of clear sky and missing joint histograms. The CRs themselves are shown in the [appendix](#).

Full name	Acronym	CR member(s)	DJF			JJA		
			Ocean	Land	Total	Ocean	Land	Total
Tropical high and thick clouds	H1_tk	1, 3, 5	1.96%	0.66%	2.62%	2.03%	0.68%	2.70%
Tropical high and thin clouds	H1_tn	7, 9	2.61%	0.51%	3.12%	2.16%	0.36%	2.52%
Extratropical high and thick clouds	H2_tk	2, 6	4.32%	1.57%	5.89%	3.95%	1.57%	5.52%
Extratropical high and thin clouds	H2_tn	8	3.28%	1.03%	4.30%	3.30%	0.84%	4.14%
Mid level clouds	Mid	4, 15A, 15B	6.70%	3.60%	10.30%	5.43%	3.01%	8.44%
Low and thick clouds	L_tk	10, 11, 12, 13	13.36%	2.13%	15.49%	12.99%	2.57%	15.56%
Low and thin clouds	L_tn	14	14.37%	1.11%	15.47%	12.20%	1.26%	13.47%
Semi clear clouds	S-Clr	15C	25.49%	12.00%	37.49%	29.07%	11.46%	40.53%
Clear-sky and missing	CS+Ms	—	1.52%	3.79%	5.31%	2.48%	4.63%	7.11%
Sum			73.6%	26.4%	100.0%	73.6%	26.4%	100.0%

JJA than DJF (Figs. 2c,f) as indicated by the light color circles corresponding to later years congregating more at higher temperatures (right side) in the former case.

b. Decomposition of CRE feedback by CR groups

Following Eq. (1) in Z23, the decomposition of CRE (X) by cloud regime (which also applies to our CR groups) is represented as

$$X = \sum_{r=1}^R f_r X_r, \quad (3)$$

where f_r and X_r represent the RFO and the average of X within the grid cells belonging to a group r . Similar to the linear regression in Eq. (2), a CR group's contribution to CRE can also be represented by a linear regression:

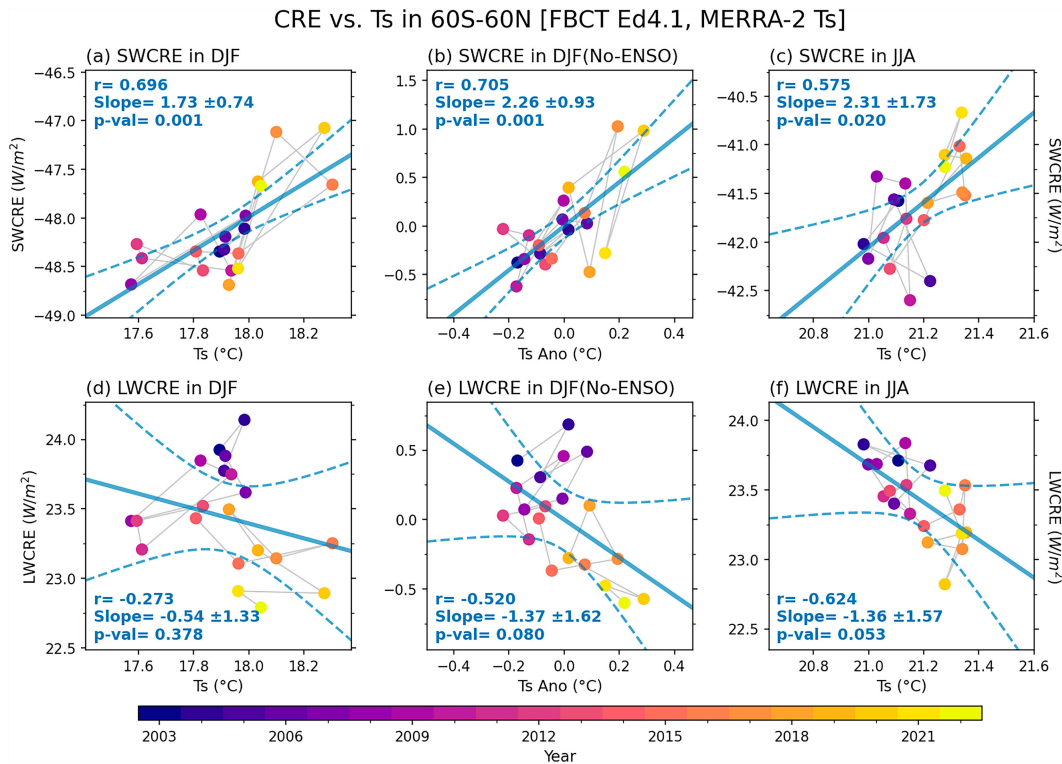


FIG. 2. (a)–(c) SWCRE vs domain mean surface temperature (T_s) in 60°S–60°N for DJF, No-ENSO DJF, and JJA seasonal means, and (d)–(f) LWCRE vs T_s . Blue solid lines are regression lines of SW/LWCRE against T_s and blue dashed curves show the 5%–95% range of the regression mean. Correlation coefficients (r), regression slope uncertainties in the 5%–95% range, and p values are provided in each panel. Each year is represented by a different symbol color according to the color bar at the bottom and light gray lines connect consecutive year symbols.

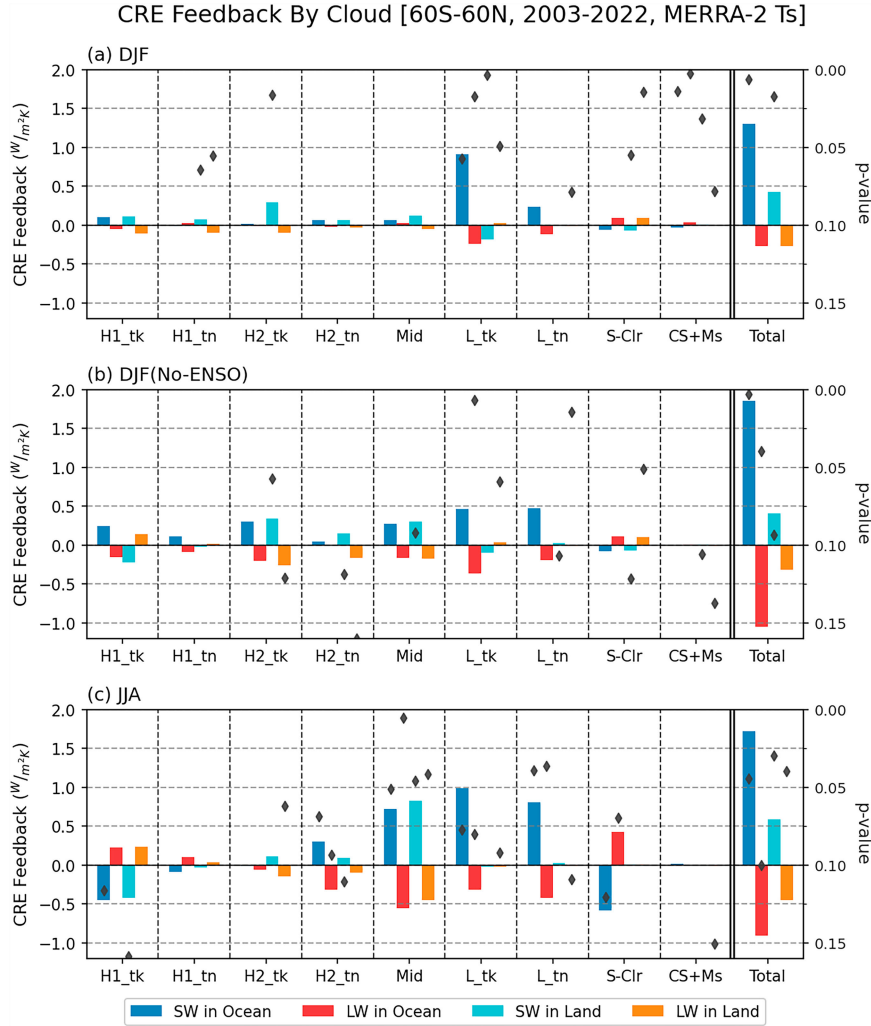


FIG. 3. Decomposition of CRE feedback by CR groups in (a) DJF, (b) No-ENSO DJF, and (c) JJA. SWCRE feedback over ocean (dark blue) and land (light blue), and LWCRE feedback over ocean (red) and land (orange). The rightmost column (“Total”) shows sums of each term for all CR groups and “CS+Ms” grid cells. Diamond symbols show the corresponding regression p value along the secondary y axis on the right side (only if the p value is less than 0.16).

$$f_r X_r = \alpha_r T_s + \beta_r + \epsilon_r. \quad (4)$$

Using Eqs. (2) and (4), Eq. (3) transforms to

$$\begin{aligned}
 X &= \alpha T_s + \beta + \epsilon = \sum_{r=1}^R (\alpha_r T_s + \beta_r + \epsilon_r) \\
 &= T_s \sum_{r=1}^R \alpha_r + \sum_{r=1}^R \beta_r + \sum_{r=1}^R \epsilon_r. \quad (5)
 \end{aligned}$$

Hence, the total CRE feedback (α) is the sum of CRE feedbacks by individual CR groups (α_r).

Figure 3 shows the contribution to SWCRE/LWCRE feedback of each CR group and reveals a distinct contrast between the two seasons. In DJF, total CRE feedback is dominated by

positive SWCRE feedback (less reflection of SW) in oceanic low-thick (L_{tk}) clouds (p value < 0.06; Fig. 3a). Continental second-highest thick (H2_{tk}) and oceanic low-thin (L_{tn}) clouds also show measurable contributions, but their magnitudes are about a quarter or less than those of oceanic low-thick clouds. LWCRE feedbacks in DJF are mostly weak. On the other hand, a more diverse mixture of clouds contributes to SWCRE/LWCRE feedbacks both positively and negatively in boreal summer (Fig. 3c). For example, similarly large positive SWCRE feedbacks are reported by oceanic Mid, L_{tk}, and L_{tn} clouds and continental Mid clouds (all p values < 0.08) while notable negative feedbacks are contributed by tropical convective clouds (H1_{tk}) over ocean and land, and sparse clouds (S-Clr) over ocean (but with p values slightly over 0.1). The across-group variability of LWCRE feedback in JJA is similar to that of SWCRE feedback, but with opposite sign. The SWCRE

(LWCRE) feedback decomposition in JJA indicates less reflection of SW (more escape of LW) by various clouds, while H1_tk and S-Clr clouds reflect SW (trap LW) more as surface warms.

The contrast between DJF and JJA seasons is intriguing and requires more in-depth analysis. The following subsection shows such an analysis, specifically whether CRE feedbacks are due to the changes in CR group cloud properties or due to the changes in their RFO.

c. Further decomposition for cloud property change versus occurrence frequency change

As shown in Z23's Eq. (2), X anomalies can be decomposed to three terms per CR group, namely due to the changes in cloud property, changes in RFO, and their covariance. When Z23's Eq. (2) is applied to our Eq. (3)

$$\Delta X = \sum_{r=1}^R (\bar{f}_r \Delta X_r + \Delta f_r \bar{X}_r + \Delta f_r \Delta X_r). \quad (6)$$

Equation (6) indicates that the total CRE change ΔX consists of within-group (or internal) CRE changes ΔX_r multiplied by mean RFO \bar{f}_r and CR group RFO changes Δf_r multiplied by mean CRE \bar{X}_r ; covariances (the third term on the RHS) are usually small. In the context of CRE feedback, Eq. (6) can be rewritten as

$$\begin{aligned} \frac{\partial X}{\partial T_s} &= \alpha = \sum_{r=1}^R \alpha_r \\ &= \sum_{r=1}^R \left(\bar{f}_r \frac{\partial X_r}{\partial T_s} + \frac{\partial f_r}{\partial T_s} \bar{X}_r + \frac{\partial f_r}{\partial T_s} \frac{\partial X_r}{\partial T_s} \right), \end{aligned} \quad (7)$$

where the interpretation of the right-hand side is essentially the same as in Eq. (6).

An example of how Eq. (7) can be visually conveyed is provided in Fig. 4 for oceanic SWCRE feedback. Other SWCRE and LWCRE results are shown in Figs. S3–S5. Consistent with Fig. 3a, the results in DJF (Fig. 4a) show dominant signal of L_tk clouds for oceanic SWCRE feedback, and, moreover, most of the positive feedback of these clouds comes from RFO changes (green bars; i.e., decreased occurrence of L_tk clouds with warming weighted by negative mean SWCRE). Notable signals due to the RFO changes also occur in JJA (Fig. 4c). During that season, tropical convective clouds (H1_tk) and sparse clouds (S-Clr) exhibit negative feedback while Mid and low clouds (L_tk and L_tn) exhibit positive feedback, with the RFO component being dominant with p value < 0.1 except for the L_tk clouds (more details about the CRE feedback of this group are examined in section 4b). However, it is worth noting that while the individual within-group CRE change terms are small, they are mostly of the same sign, which results in a larger total CRE feedback than that due to RFO change terms.

Beyond these oceanic SWCRE feedbacks, we likewise generally find that the RFO-change terms $\Delta f_r \bar{X}_r$ are larger than the internal CRE-change terms for these CR groups except for L_tk (Figs. S3–S5), although the individual RFO terms are often competing with opposite signs. For example, for the continental SWCRE feedback in JJA, the positive contribution of the Mid clouds' RFO-change term is compensated by the negative RFO-change term of tropical convective clouds (H1_tk). Again, the magnitudes of the internal CRE-change term $\bar{f}_r \Delta X_r$ for individual CR groups are much smaller than those of the RFO-change terms, but the “no-offset” feature results in a larger total CRE feedback.

To investigate further the RFO change, we applied the same linear regression against T_s , but to the DJF and JJA mean RFO maps of each CR group (Figs. 5 and 6, respectively). In DJF, tropical high clouds [H1_tk (Fig. 5a) and H1_tn (Fig. 5b)] commonly show typical ENSO responses: negative signals in the Maritime Continent and positive signals in the central-to-eastern equatorial Pacific. The L_tn (Fig. 5g) and S-Clr (Fig. 5h) clouds also exhibit an organized pattern with opposite signs compared to tropical high clouds, mostly consistent with Park and Leovy (2004). Over ocean, three CR groups show large domain mean RFO response to T_s : L_tk ($-1.0\% \text{ K}^{-1}$), L_tn ($-0.8\% \text{ K}^{-1}$), and S-Clr ($1.6\% \text{ K}^{-1}$). Considering that the global sum CR group RFOs should always be 1 (=100% when including CS+Ms grid cells), it appears that the increase of S-Clr clouds is compensated by the decrease of L_tk and L_tn clouds with warming. However, Fig. 4a showed that the positive feedback by the RFO-change term of L_tk clouds is much larger than the feedback due to the same term by L_tn and S-Clr clouds. This is because when the mean CRE of L_tk clouds is weighted to the RFO change [Eq. (7)], it is much larger than that of the other two CR groups (Fig. S1).

The RFO responses to T_s are much more varied in JJA. L_tn (Fig. 6g) and S-Clr (Fig. 6h) clouds show surprisingly large responses over ocean, but with opposite sign ($-5.0\% \text{ K}^{-1}$ and $6.3\% \text{ K}^{-1}$, respectively), which partially cancels out their contribution to the total CRE feedback (Fig. 4c). In Fig. 4c, the RFO-change terms of H1_tk and Mid clouds are also notable, but the RFO changes themselves of these clouds are rather smaller ($0.5\% \text{ K}^{-1}$ and $-1.18\% \text{ K}^{-1}$, respectively). As is the case for L_tk clouds in DJF, the relatively large mean CREs of these CR groups explain this apparent discrepancy. Based on these RFO responses to T_s , and considering the characteristics of RFO, we hypothesize a systematic transition of clouds from one group to another has occurred as T_s rises, something we discuss in section 4c.

4. Discussion

a. The role of ENSO in boreal winter

Using our decomposition, we found that total CRE feedback in DJF is dominated by the positive SWCRE feedback caused by fewer oceanic L_tk clouds under warming. This result is consistent with several previous model-based studies

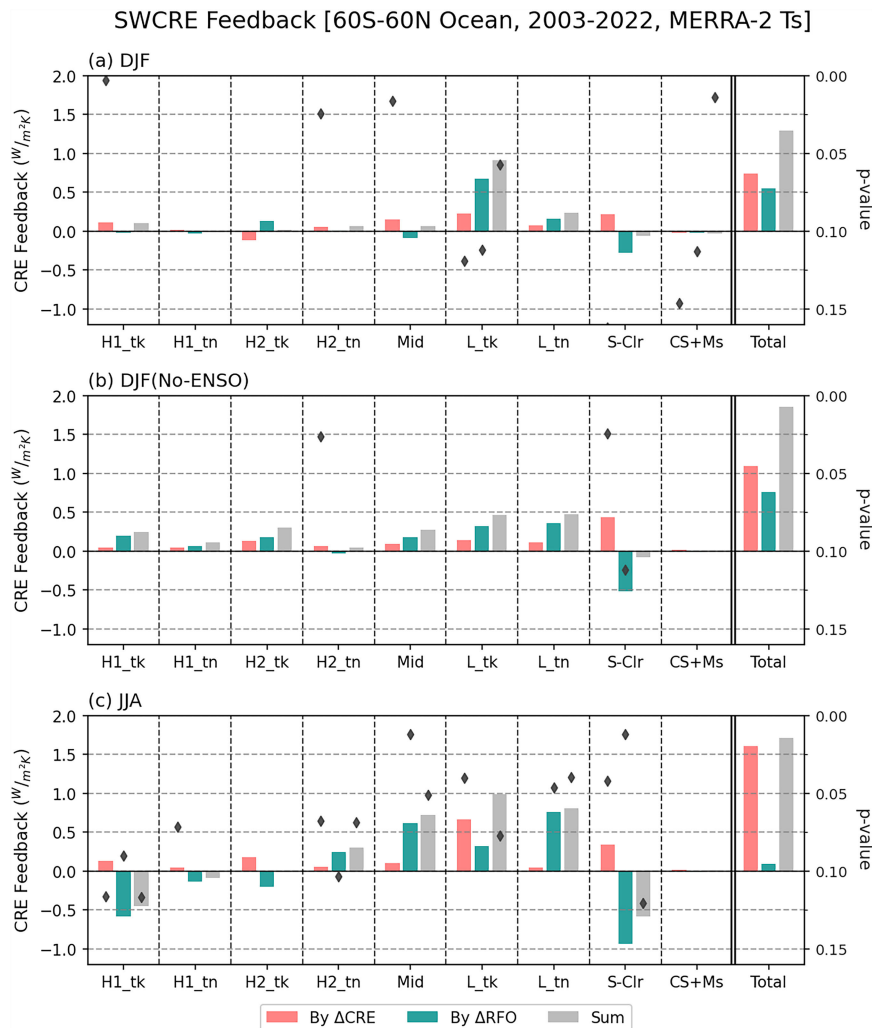


FIG. 4. Decomposition of oceanic SWCRE feedback by CR groups and by (internal) “CRE change” (dark red) and “RFO change” (dark green) terms for (a) DJF, (b) No-ENSO DJF, and (c) JJA. The (typically small) covariance term in Eq. (7) is not shown here, but the gray bar is actually the sum of all three terms. As in Fig. 3, the p value is marked with the gray diamond symbol, and the rightmost column (“Total”) shows sums of each term for all CR groups (thus p values are unavailable for the “Total” column).

(e.g., Koshiro et al. 2022; Zelinka et al. 2016). However, such CRE feedback behavior is limited to DJF, which raises the possibility that seasonal characteristics strongly affect the feedback signal.

Boreal winter is known for peak ENSO activity. ENSO is a strong interannual variability affecting the globe by setting a distinctive SST pattern, which modulates notable anomalies in TOA radiation budget. This is reminiscent of the “SST pattern effect” (Stevens et al. 2016), which is the term used for describing how a spatial pattern of SST driven by global warming shapes global cloud feedback, and which has generally been studied at multidecadal time scales (e.g., Andrews et al. 2015; Zhou et al. 2016). At short time scales of less than two decades, as in this study, the ENSO-driven short-lived SST pattern can significantly affect the CRE feedback,

making it comparable to the global warming signal itself (Ceppi and Fueglistaler 2021; Zhou et al. 2015). This is particularly true for our study period which includes the historically strong El Niño event of 2015/16.

We tested various aspects of the effect of ENSO on CRE feedback, and found the effects to be rather intricate. First, we tested relationships among CRE, T_s , and ENSO indices and produced figures similar to Fig. 2. Figures S6 and S7 show that ENSO indices and T_s correlate strongly in DJF (coefficients close to 0.7 with p value 0.001), but this is not true when the relationships between near-global mean SWCRE/LWCRE and ENSO indices are examined (coefficient magnitudes are below 0.3 and insignificant at the 90% confidence level). These two correlation analyses indicate that the direct impact of ENSO on the near-global mean CRE is relatively

Seasonal Mean RFO regressed against T_s
(Cld_k15, MERRA-2 T_s , 60S-60N, 2003-2022 DJF)

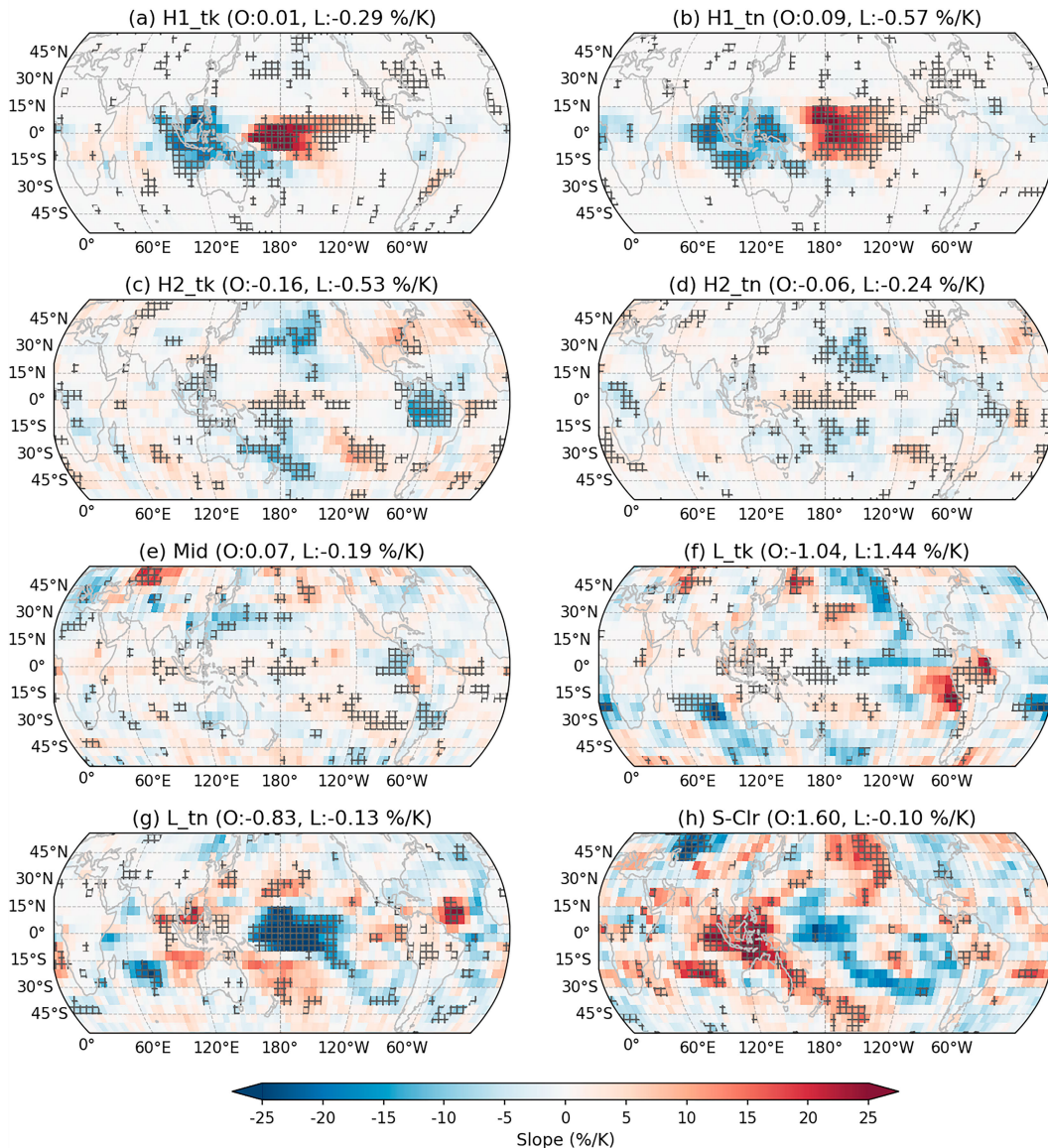


FIG. 5. Boreal winter seasonal mean RFO of each CR group regressed against T_s , after degrading the original 1° grid cell to 5° resolution. The weighted domain mean of regression slopes is provided above each panel for ocean and land separately. Hatched areas indicate regression p values of smaller or equal to 0.05.

weak, suggesting compensating effects among various CR groups regionally. We also tested a Fig. 5-like RFO response map to the Niño-3.4 index (Fig. S8) to gauge how cloud occurrences respond to ENSO. Consistent with the strong correlation between T_s and the Niño-3.4 index, Fig. S8 is essentially the same as Fig. 5. This means that an ENSO-induced SST pattern sets the boreal winter cloud occurrence pattern.

To examine the CRE compensations due to ENSO responses, we performed the decomposition of ENSO effect on CRE by replacing T_s in Eqs. (5), and (7) with the Niño-3.4

index, and producing figures similar to Figs. 3 and 4; that is, we decomposed the CRE response to ENSO into contributions from RFO and internal cloud changes (Figs. S9 and S10). These figures show that the oceanic SWCRE changes directly related to ENSO are dominated by L_tk clouds, mostly because of RFO changes (Park and Leovy 2004; Zhu et al. 2007). This contribution pattern of L_tk clouds is nearly identical to the results of Figs. 3a and 4a, further highlighting the significant influence of ENSO on the DJF CRE feedback. We note that the dominant response of L_tk clouds to ENSO is maintained regardless of season (Figs. S9 and S10),

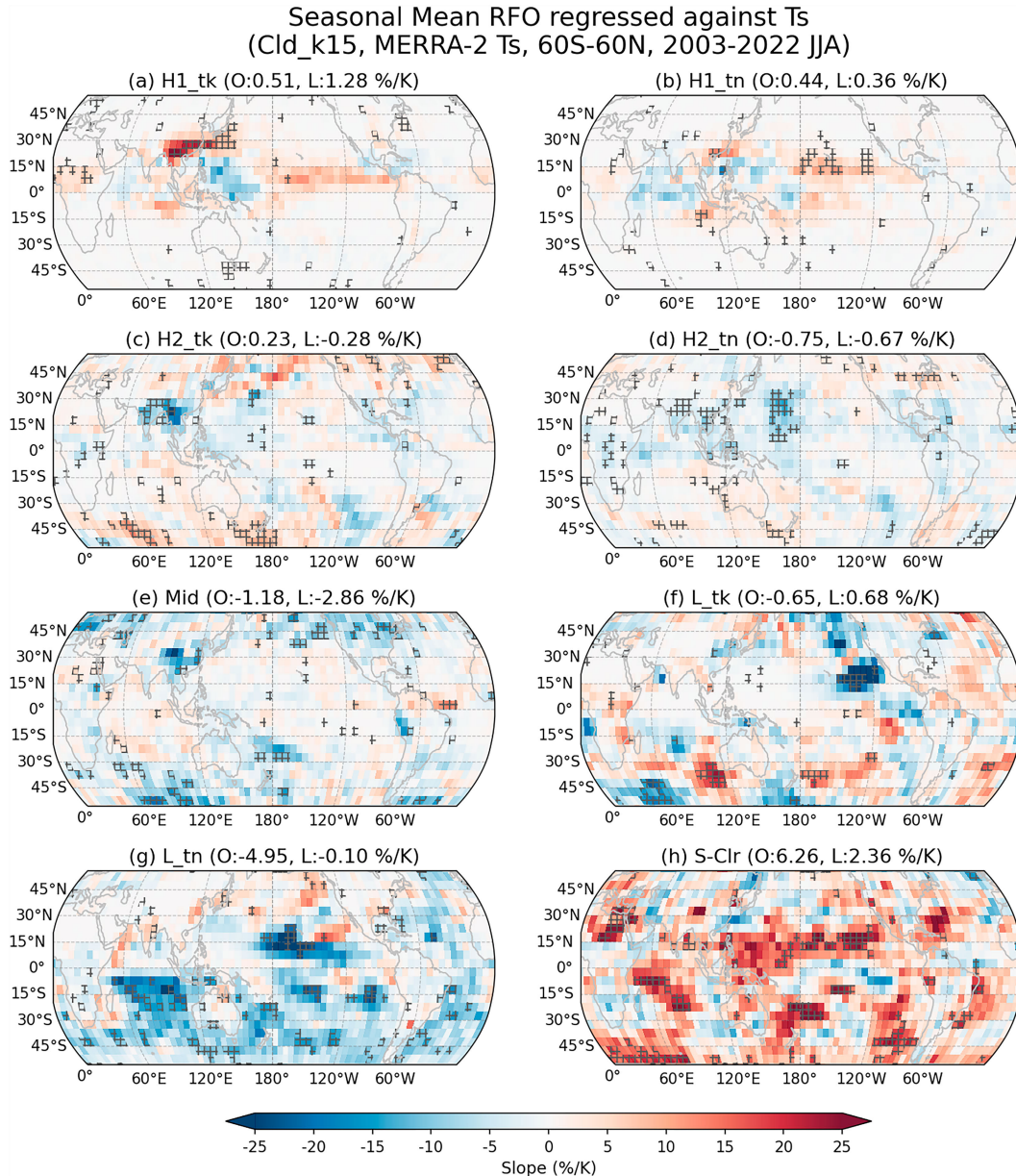


FIG. 6. As in Fig. 5, but for boreal summer.

supporting the consistent prevalence of ENSO effects. However, JJA CRE feedback patterns shown in Figs. 3c and 4c are different from those of the ENSO-only CRE responses, probably due to the weakened ENSO in boreal summer. On the other hand, besides the individual CR group responses, the total CRE response to ENSO for all clouds shown in the rightmost column is notably different between Fig. 3a and Fig. S9a. In the case of the CRE response to ENSO, the large positive signal of L_{tk} clouds is compensated by other clouds, thus resulting in much smaller feedback overall, while Fig. 3 showed larger total feedback than that from the L_{tk} group alone. This indicates that the redistribution of clouds by ENSO does not create large global mean CRE anomalies

due to offsets, which may be related to the weaker correlation between near-global mean CRE and ENSO indices shown in Fig. S7.

To study these issues further, we conducted an additional decomposition (namely, “No-ENSO”) where the ENSO signal was removed from T_s seasonal means before recalculating the CRE feedback (i.e., using residuals after linear regression against the Niño-3.4 index). The DJF result is presented in Figs. 2b, 2e, 3b, and 4b, while the JJA result is omitted since there is no qualitative difference between original and No-ENSO CRE feedbacks (i.e., the effect of ENSO in boreal summer is weak to begin with). In terms of near-global mean CRE feedback, the magnitudes of both SWCRE and LWCRE feedback are enhanced in DJF. For example, in

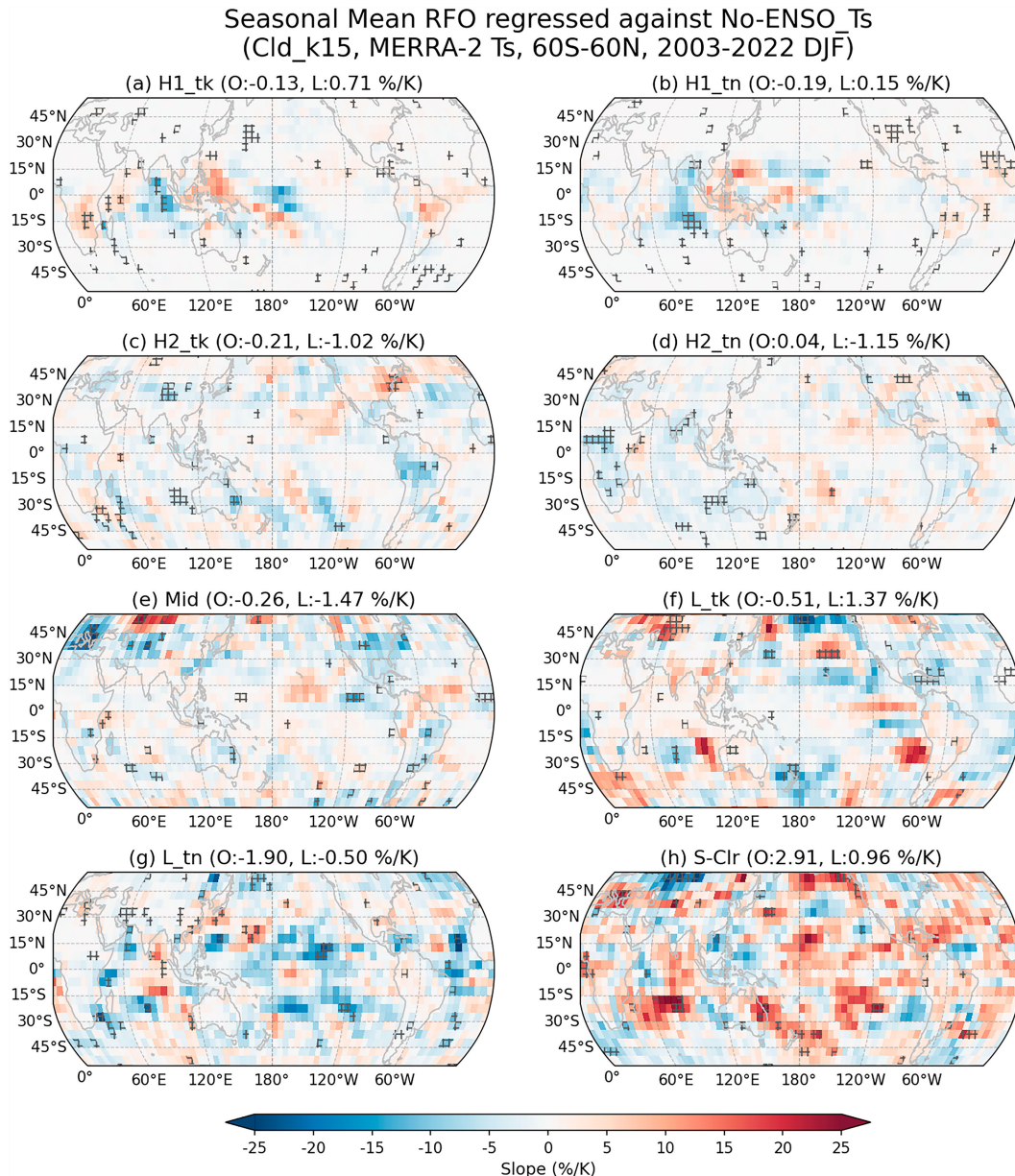


FIG. 7. As in Fig. 5, but with RFO regressed against No-ENSO T_s , where the regression of T_s against the Niño-3.4 index is subtracted.

Figs. 2b and 2e, SWCRE feedback increases from 1.73 to 2.26, and LWCRE feedback also strengthens from -0.54 to -1.37 , when the ENSO signal is excluded. In the case of LWCRE, the correlation becomes much stronger (-0.27 to -0.52), and the p value decreases below 0.1. The contribution pattern by CR groups also dramatically changes (Fig. 3b); the dominant role in oceanic SWCRE feedback of L_tk clouds disappears and various CR groups contribute equitably to the total cloud feedback, particularly for both oceanic SWCRE and LWCRE (e.g., H1_tk, H2_tk, Mid, and L_tn). In addition, these oceanic feedback signals are mostly accompanied by high p values indicating increased uncertainty. The decomposition

figure (Fig. 4b) shows that the magnitudes of RFO-change terms are generally larger than those of CRE-change terms, but also come with high p values, warranting future study with longer time series.

One interesting point here is that the RFO contribution to oceanic SWCRE feedbacks is positive for most CR groups except S-Clr clouds (Fig. 4b). Considering the relatively weak mean SWCRE of S-Clr clouds, a significant increase of S-Clr RFO is expected globally. We produced the same figure of RFO trend map as Fig. 5, but with No-ENSO T_s , and found that the RFO of S-Clr clouds increases at the rate of $2.91\% \text{ K}^{-1}$ over ocean (Fig. 7h). This indicates that global

warming may suppress the occurrence of thicker or higher clouds, but lead to an increase of cloud-sparse scenes in boreal winter ocean, if the effect of ENSO weakens, although the statistical significance of RFO change with No-ENSO T_s is rather weak. Overall, the global distributions of positive and negative RFO signals of CR groups in the no-ENSO regression of Fig. 7 seem far noisier than those in Figs. 5 and 6. Last, it is worth noting that, in Fig. 4b, the oceanic SWCRE contribution of S-Clr clouds is actually small because the large negative RFO-change term is compensated by the positive internal CRE-change term, which means that S-Clr clouds become thinner or of smaller cloud fraction (CF) with higher T_s . This internally changing feature of S-Clr clouds is also noticeable in JJA (both p values are less than 0.05), and its details are examined in the next subsection.

Returning to L_{tk} clouds, our results can be interpreted as showing that the higher T_s in El Niño conditions coincide with fewer oceanic low-thick clouds, which results in more absorption of SW radiation. The regions of notable negative RFO trend of L_{tk} clouds include the equatorial eastern Pacific, northeastern Pacific, southeastern Indian Ocean, and southeastern Atlantic Ocean (Fig. 5f). Among them, it is interesting that, when RFO is regressed against No-ENSO T_s , the signals flip in the equatorial eastern Pacific and southeastern Indian Ocean while the signal in the southeastern Atlantic Ocean remains consistently negative (Fig. 7f). The details of these regional differences merit further examination in future studies. In addition, the northeastern Pacific also deserves special attention. The negative RFO signal of L_{tk} clouds implies warmer SST in this area. Actually, a notable event colloquially named “the Blob” occurred in 2013–15 (Bond et al. 2015; Di Lorenzo and Mantua 2016). This event was characterized by abnormally positive SST anomalies persisting for multiple years, and then ultimately interacting with the strong 2015/16 El Niño (Santoso et al. 2017; Tseng et al. 2017). In a relatively short (20 years) study period like ours, such a notable regional event can distort the global mean CRE feedback, but currently we cannot be sure whether “the Blob” was a random abnormal event or a global warming signal.

Last, we also tested the relationship between the Pacific decadal oscillation (PDO; Mantua et al. 1997) and T_s since Loeb et al. (2021) suggested a possible link between PDO and decadal changes in the Earth’s energy budget. However, we found the relationship between PDO and T_s to be much weaker than that with ENSO (Figs. S6 and S7) echoing recent work by Raghuraman et al. (2023), who found a weak relationship between PDO and CRE on a global-mean scale.

b. Internal cloud changes within CR groups

In the previous section, we found statistically significant signals of internal CRE-change term in SWCRE feedback for oceanic L_{tk} in JJA and S-Clr clouds in both JJA and No-ENSO DJF. To investigate this, we performed a regression against T_s of the binned CFs of the JJA seasonal mean CR group joint histograms (Fig. 8; DJF counterparts with T_s and No-ENSO T_s are shown in Figs. S11 and S12,

respectively). We performed such an analysis because CR group-mean CRE changes should be related to changes in the clouds’ mean joint histogram (Zelinka et al. 2012a,b, 2016, 2023). As expected, the decrease of SW reflection for L_{tk} and S-Clr clouds with warming appears to be due to the decrease of their CF (-2.81% and $-1.64\% \text{ K}^{-1}$, respectively). Moreover, regression slopes of individual binned CFs indicate that L_{tk} clouds become optically thinner on average (increasing in thinner bins while decreasing in thicker bins in Fig. 8f), which amplifies the reduction of SW reflection. When examining regression slopes of binned CFs for individual regimes in the L_{tk} group (Figs. 8i–l), we found that the thinning trend is more notable in CR10 and CR11, while the reduction in total CF is stronger in CR12 and CR13. The thinning trends of CR10 and CR11 are also noticeable in DJF oceans, but decreasing CF trends are much weaker, with both T_s and No-ENSO T_s (Figs. S11 and S12), thus the smaller feedback contribution of the internal CRE-change term with weaker significance in Figs. 4a and 4b. In the case of S-Clr clouds, mean SWCRE itself is relatively small, hence the change of CF at 1% – $2\% \text{ K}^{-1}$ does not result in a notable change of SWCRE. However, the overwhelming RFO of S-Clr clouds amplifies the effect of even a small within-group SWCRE change.

On the other hand, L_{tn} cloud also shows overall negative regression slope of binned CF ($-0.98\% \text{ K}^{-1}$), but individual binned CF slopes show a thickening trend with a transition from the thinnest bin to the thicker bins (Fig. 8g). Hence, the near-zero feedback by CRE-change term of L_{tn} clouds in Fig. 4c can be interpreted as an offset between decreasing CF and thickening clouds. In addition, notable negative slopes in cirrus clouds are detected in H1_{tn} and H2_{tn} clouds (Figs. 8b,d). However, the decomposition of LWCRE feedback over ocean shows the absolute magnitudes of the internal CRE-change term in H1_{tn} and H2_{tn} clouds to be quite small (the CRE-change term in H1_{tn} clouds is of very small p value, though; Fig. S4c). This is partially because of weighting by the relatively small mean RFOs of the H1_{tn} and H2_{tn} groups (about 3% and 4%, respectively; Table 1). When we tested the same regression analysis on cloud histograms of all grid cells (i.e., all CRs combined; Figs. S13 against T_s and S14 against No-ENSO T_s), the regression slope patterns were similar to that of S-Clr (Fig. 8h) regardless of season, due to the dominant RFO of the S-Clr group, while regression slopes in other bins were near zero.

c. Hemispherical contrast and regional characteristics

In addition to the asymmetric seasonal strength of ENSO, the combination of seasonally changing insolation and uneven distribution of land and ocean can contribute to the hemispherical differences of CRE feedback. To examine this issue, we produced the Fig. 3–like plot of CRE feedback decomposition, but for the Northern Hemisphere (NH) and Southern Hemisphere (SH) separately for each season (Fig. S15). We note that the same near-global mean T_s is used in Fig. S15 as in Figs. 3a and 3c, and No-ENSO T_s version is presented in Fig. S16.

Seasonal Mean Histogram regressed against T_s
[Cld_k15, MERRA-2 T_s , 60S-60N Ocean, 2003-2022 JJA]

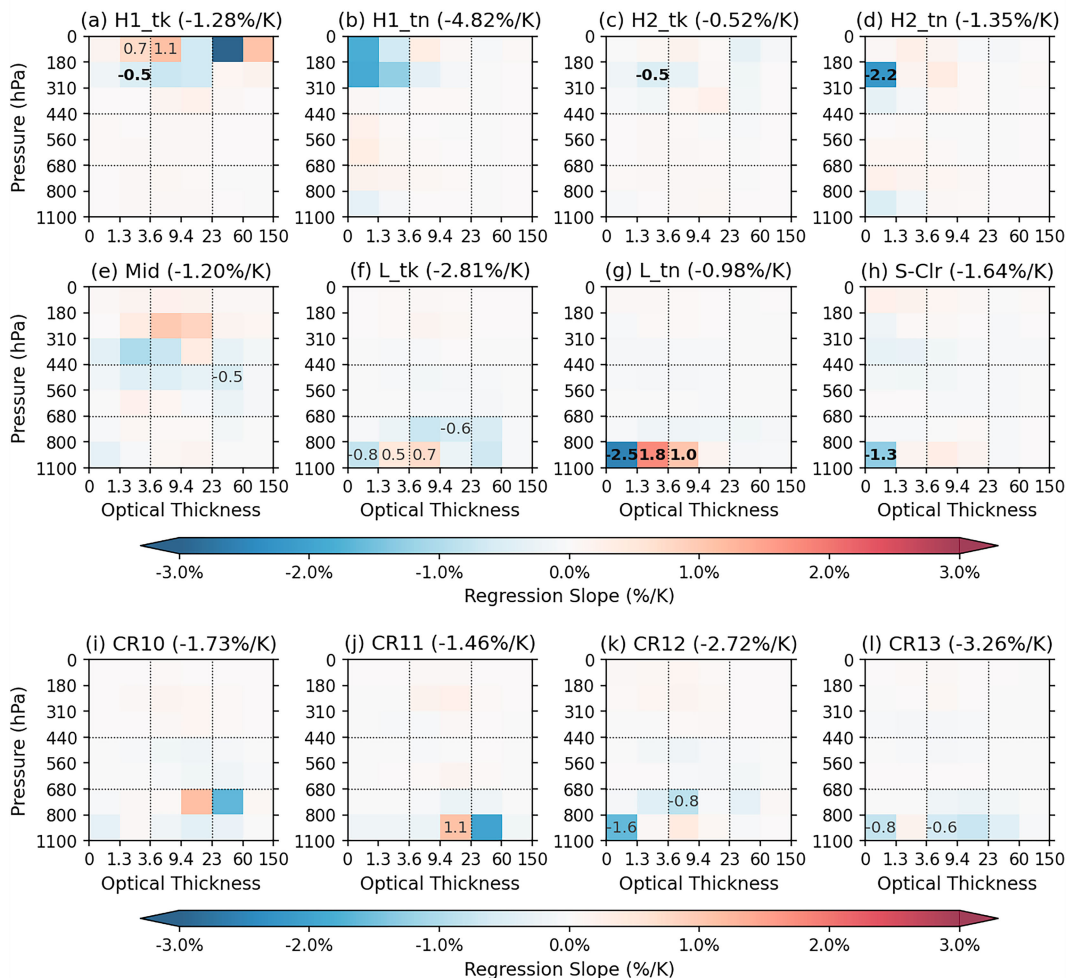


FIG. 8. (top),(middle) Slopes of oceanic boreal summer seasonal mean joint histogram binned CFs of each CR group when regressed against T_s . (bottom) The same slopes of binned CFs, but for individual CRs of the L_tk group. The sum of binned CF regression slopes is given above each panel. Slopes larger than 0.5 are explicitly shown when the corresponding p value is below 0.1 (and in boldface when the p value is below 0.05).

In boreal winter (Figs. S15a,d), the positive CRE feedback by oceanic L_tk clouds is commonly seen in both hemispheres, but with larger magnitude in the SH. The larger CRE due to larger insolation in summer hemisphere and larger mean RFO of L_tk clouds in the SH may contribute to this result. One interesting point is that the CRE feedback signals by $H2_tk$ and Mid clouds in DJF cancel out between the NH and SH. For example, positive SWCRE feedback by oceanic $H2_tk$ and Mid clouds in the NH (winter hemisphere) is being offset by negative feedback in the SH (summer hemisphere). The opposite signs of feedback signals are mostly related to the RFO-change term (not shown), yielding thus overall small feedback in Fig. 4a. In the decomposition based on No-ENSO T_s , oceanic SWCRE and LWCRE feedback signals of these two cloud groups in the SH flip over to positive, while those in the NH remain same, reflecting the hemispherically asymmetric effect of ENSO (e.g., Jin and Kirtman 2009).

The boreal summer season also shows hemispherical differences. First, notable SWCRE feedbacks over land are seen in the NH ($H1_Tk$ and Mid clouds) but not in the SH. In the SH, oceanic Mid, L_tn , and S-Clr clouds contribute most of CRE feedbacks, which is different from the NH where L_tk and $H1_tk$ clouds exhibit sizable signals. The comparisons between hemispheres for their common local season (e.g., NH in DJF versus SH in JJA or vice versa) also show dramatically different CRE feedback patterns.

These regional differences and the fact that most CRE feedbacks are due to the RFO change motivated us to examine regionally detailed RFO trends of CR groups. Hence, we derived regression slopes of JJA zonal mean RFOs against T_s for every 15° in latitudes (Fig. 9), representing the tropics (0°–15°), subtropics (15°–30°), midlatitudes (30°–45°), and high latitudes (45°–60°) of each hemisphere. The DJF counterpart is presented in Figs. S17 (against T_s) and S18 (against No-ENSO T_s).

insight into the seasonal characteristics of CRE feedback even with a limited number of samples.

We found that SWCRE feedback by oceanic low-thick (L_{tk}) clouds dominates global CRE feedback during DJF, and particularly the decreasing RFO of L_{tk} clouds with surface warming yields positive SWCRE feedback. We also accounted for the effect of ENSO on this CRE feedback since ENSO sets up a unique spatial distribution pattern of SST, which perhaps can be used as a proxy for the so-called pattern effect on CRE feedback. When doing so, the dominance of SWCRE feedback by L_{tk} clouds seemed to most likely originate from ENSO. ENSO also disturbs LWCRE feedback by reducing its magnitude, and results in weaker correlation between LWCRE and T_s .

During the JJA season, we found notable signals in the within-group CRE change term for oceanic L_{tk} and sparse (S-Clr) clouds. Further regression analysis of cloud fraction distributions against T_s showed that both the thinning of clouds and the decrease of overall CF within CR groups can explain the internal CRE-change signal. Another characteristic of JJA feedback is that various CR groups have competing positive and negative global CRE feedbacks. For example, mid and low clouds contribute to a positive SWCRE feedback while tropical convective ($H1_{tk}$) clouds and S-Clr clouds offset it. These effects are mostly due to the decreasing and increasing RFO of corresponding CR groups with warmer T_s except the aforementioned oceanic L_{tk} and S-Clr clouds. From additional analysis of RFO change by T_s , the following two signals were found as the global warming responses:

- 1) Decreasing occurrence of cumulus resulting in larger clear-sky fractions, particularly over oceans.
- 2) Transition to higher top convective clouds in most regions except southern subtropics.

The second finding is mostly exclusive to boreal summer, while the decreasing L_{tn} and increasing S-Clr clouds are also seen in DJF with weaker magnitude.

The stronger effect of ENSO during DJF than JJA is an obvious reason for the dramatic contrast between the two seasons. When we examined the CRE feedback components with ENSO-excluded T_s , we found that the magnitudes of total CRE feedbacks are similar between DJF and JJA (Fig. 3b vs Fig. 3c). However, notable differences of CRE feedbacks between the two seasons remain if we examine details by CR group. Hence this study suggests that seasonal separation is advisable for more accurate feedback assessment. This is particularly true because it is uncertain whether ENSO's effect on CRE feedback is linear: if it is not, a model-based long-term average will not cancel out the effects of ENSO's opposite phases on CRE feedback. Considering a recent study of Williams et al. (2023) that suggests nonlinear responses of climate to tropical SSTs, a sophisticated feedback assessment accounting for ENSO effects would be warranted.

Acknowledgments. Resources supporting this work were provided by the NASA High-End Computing (HEC) Program through the NASA Center for Climate Simulation (NCCS) at Goddard Space Flight Center. LO acknowledges support

by NASA's MEaSUREs program. RK is supported by NASA's Science of Terra, Aqua and Suomi-NPP program (Grant 80NSSC21K1968) and CloudSat/CALIPSO Science program (Grant 80NSSC23K0207).

Data availability statement. The cloud-only regime dataset defined in 50°N–50°S (but assigned to 60°N–60°S domain; including centroids, CR-number-on-map, and sample code to calculate regime mean CRE) is available at <https://data.nasa.gov/Earth-Science/Cloud-Regime-for-CRE-Feedback-Study/g6w2-43cq>. Surface temperature data of MERRA-2 (tavg1_2d_slv_Nx, <https://doi.org/10.5067/VJAFPLI1CSIV>) were obtained from Goddard Earth Sciences Data and Information Services Center (GES DISC; <https://disc.gsfc.nasa.gov/>), Greenbelt, MD, USA. The Level-3 (L3) MODIS Atmosphere Daily Global Product of Terra (MOD08_D3, https://doi.org/10.5067/MODIS/MOD08_D3.061) and Aqua (MYD08_D3, https://doi.org/10.5067/MODIS/MYD08_D3.061) was obtained from the Level-1 and Atmosphere Archive and Distribution System (LAADS) Distributed Active Archive Center (DAAC; <https://ladsweb.modaps.eosdis.nasa.gov/>) in the Goddard Space Flight Center, Greenbelt, MD, USA. CERES FluxByCldType–Level 3 (https://doi.org/10.5067/Terra-Aqua/CERES/FLUXBYCLDTYP-DAY_L3.004A) and EBAF-TOA -Level 3b (https://doi.org/10.5067/TERRA-AQUA/CERES/EBAF-TOA_L3B004.1) data were obtained from the NASA Langley Research Center CERES ordering tool at <https://ceres.larc.nasa.gov/data/>.

APPENDIX

Details of Cloud Regimes

The cloud regimes (CRs) were derived from k -means clustering of ISCCP-like 2D joint histograms of MODIS COT and CTP (Collection 6.1; Platnick et al. 2017, 2018), both *Terra* and *Aqua* joint histograms in the 50°S–50°N domain from June 2014 to May 2019. Jin et al. (2021) presented detailed steps to obtain CRs like data preparation, initialization for clustering, and objective criteria for selecting optimal number of clusters ($k = 15$ in this case).

The original 15 CRs are composed of 9 high-cloud CRs, 5 low-cloud CRs, and the semiclear CR15, which includes various broken clouds of low cloud fraction (CF). A second round of clustering was applied only to the histograms assigned to CR15 and produced three sub-CRs (15A, 15B, and 15C). The major subregime of these in terms of RFO is still a low-CF CR (semiclear; CR15C), while the other two sub-CRs appear to be dominated by midlevel cloud. These total 17 CRs (including subregimes) are displayed in Fig. A1, where the CRs are organized into CR groups.

While the clustering process used distinct *Terra* and *Aqua* joint histograms (at daily 1° resolution), regime assignment for a particular grid cell was performed using the average *Terra-Aqua* joint histogram (TA_mean). This approach minimizes unassigned grid cells and ensures that the cloud classification represents daytime mean observations. Figure A2 shows the geographical distribution of relative frequency of

MODIS_C6.1 Terra&Aqua Cloud Regimes

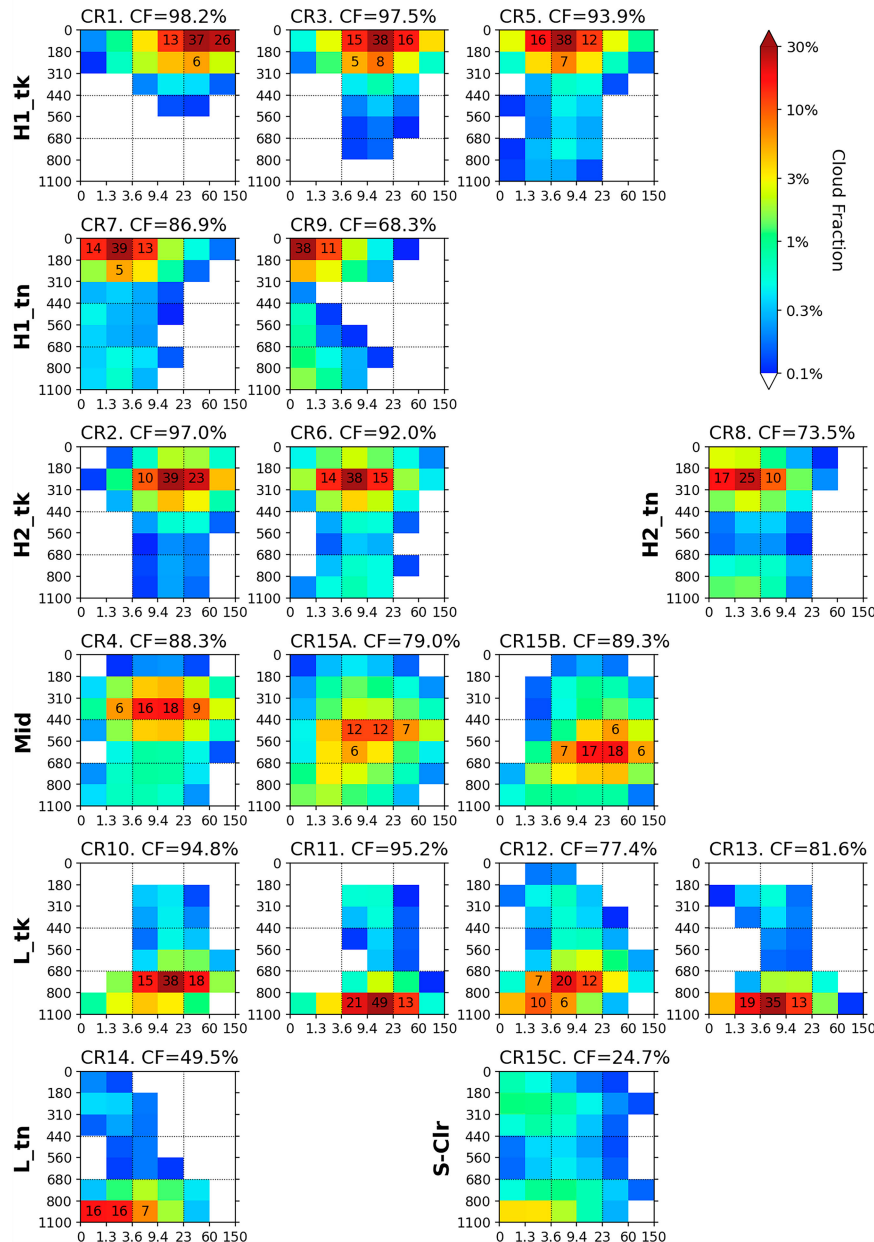


FIG. A1. Cloud regime (CR) centroid (mean histograms) that is organized into CR groups. Bin CF values exceeding 5% are shown explicitly on the centroid panels. The total CF of each CR is provided above each panel.

occurrence (RFO) of total 17 CRs including three sub-regimes of the CR15, where domain and period are set to same as those in Jin et al. (2021).

The geographical distributions of RFOs in Fig. A2 are almost identical to the original RFO distributions shown in Fig. SB5 in Jin et al. (2021). However, the nature of TA_mean histograms caused the change in mean RFO values. First, most mean RFO values increase with TA_mean histograms because the fraction

of missing grid cells decreases from about 10% to 5%, which translates to a relative 5.6% increase for each CR. However, the increase of semiclear CR15 mean RFO (31.6%–43.5%; a 37.6% relative increase) is far exceeding the level that can be explained by the decreasing missing data effect. This means that weather transitions from local morning to afternoon dilutes cloud activity that would otherwise be classified as one of the other CRs.

RFO Map of Cloud Regime assigned to TA_mean histograms [2014.06-2019.05]

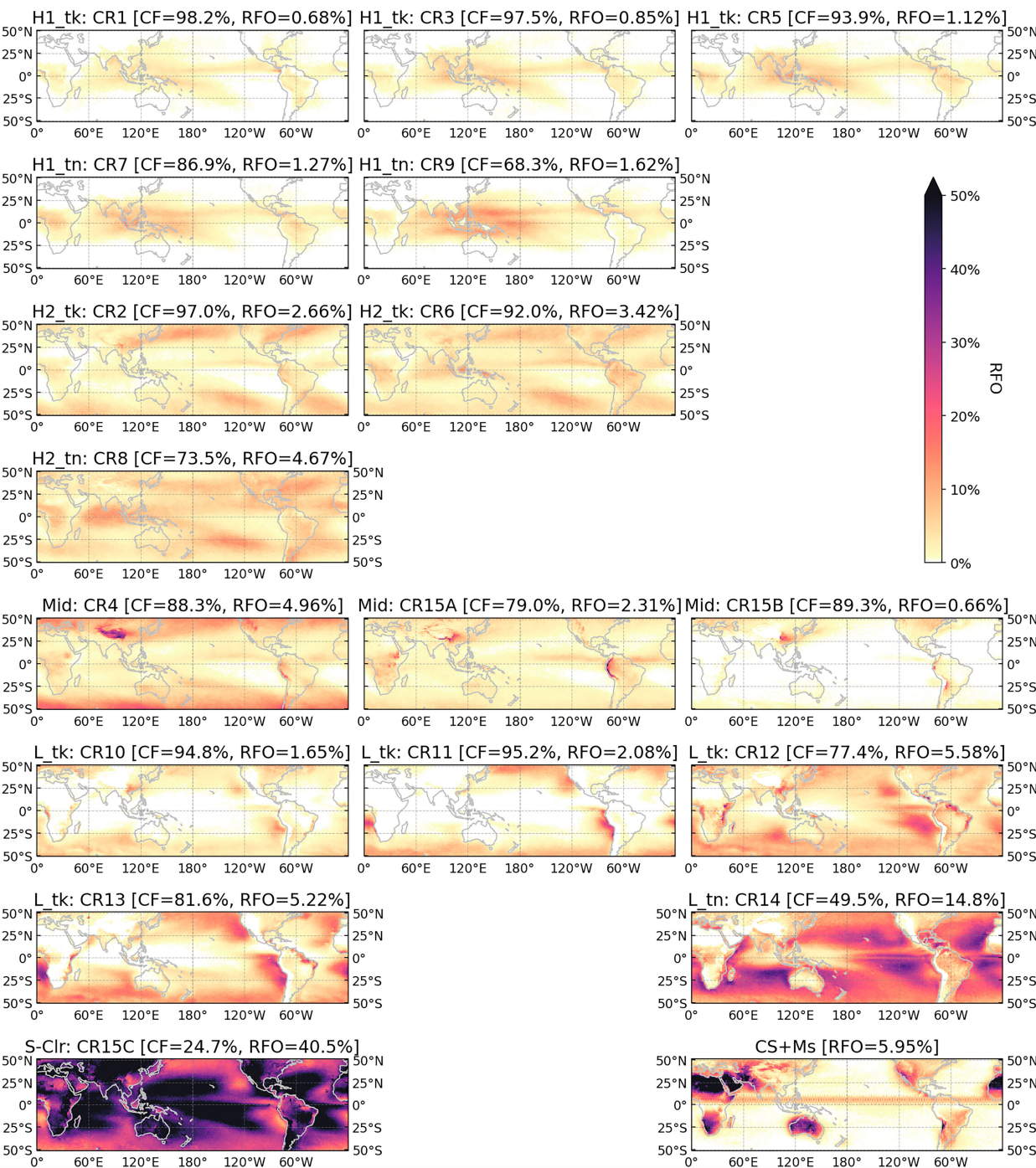


FIG. A2. Geographical distribution of relative frequency of occurrence (RFO) of each CR after *Terra–Aqua* gridcell mean histograms were assigned, and which are also rearranged as Fig. A1. CR mean RFOs are provided above the map panels.

REFERENCES

- Afyouni, S., S. M. Smith, and T. E. Nichols, 2019: Effective degrees of freedom of the Pearson's correlation coefficient under autocorrelation. *NeuroImage*, **199**, 609–625, <https://doi.org/10.1016/j.neuroimage.2019.05.011>.
- Amaya, D. J., A. J. Miller, S.-P. Xie, and Y. Kosaka, 2020: Physical drivers of the summer 2019 North Pacific marine heatwave. *Nat. Commun.*, **11**, 1903, <https://doi.org/10.1038/s41467-020-15820-w>.
- Andrews, T., J. M. Gregory, and M. J. Webb, 2015: The dependence of radiative forcing and feedback on evolving patterns of surface temperature change in climate models. *J. Climate*, **28**, 1630–1648, <https://doi.org/10.1175/JCLI-D-14-00545.1>.
- Bodas-Salcedo, A., and Coauthors, 2011: COSP: Satellite simulation software for model assessment. *Bull. Amer. Meteor. Soc.*, **92**, 1023–1043, <https://doi.org/10.1175/2011BAMS2856.1>.
- Bond, N. A., M. F. Cronin, H. Freeland, and N. Mantua, 2015: Causes and impacts of the 2014 warm anomaly in the NE Pacific. *Geophys. Res. Lett.*, **42**, 3414–3420, <https://doi.org/10.1002/2015GL063306>.
- Bony, S., A. Semie, R. J. Kramer, B. Soden, A. M. Tompkins, and K. A. Emanuel, 2020: Observed modulation of the tropical radiation budget by deep convective organization and lower-tropospheric stability. *AGU Adv.*, **1**, e2019AV000155, <https://doi.org/10.1029/2019AV000155>.
- Byrne, M. P., A. G. Pendergrass, A. D. Rapp, and K. R. Wodzicki, 2018: Response of the intertropical convergence zone to climate change: Location, width, and strength. *Curr. Climate Change Rep.*, **4**, 355–370, <https://doi.org/10.1007/s40641-018-0110-5>.
- Capotondi, A., M. Newman, T. Xu, and E. Di Lorenzo, 2022: An optimal precursor of northeast Pacific marine heatwaves and central Pacific El Niño events. *Geophys. Res. Lett.*, **49**, e2021GL097350, <https://doi.org/10.1029/2021GL097350>.
- Ceppi, P., and S. Fueglistaler, 2021: The El Niño–Southern Oscillation pattern effect. *Geophys. Res. Lett.*, **48**, e2021GL095261, <https://doi.org/10.1029/2021GL095261>.
- Cess, R. D., and Coauthors, 1990: Intercomparison and interpretation of climate feedback processes in 19 atmospheric general circulation models. *J. Geophys. Res.*, **95**, 16 601–16 615, <https://doi.org/10.1029/JD095iD10p16601>.
- , and Coauthors, 1996: Cloud feedback in atmospheric general circulation models: An update. *J. Geophys. Res.*, **101**, 12 791–12 794, <https://doi.org/10.1029/96JD00822>.
- Chung, E.-S., and B. J. Soden, 2018: On the compensation between cloud feedback and cloud adjustment in climate models. *Climate Dyn.*, **50**, 1267–1276, <https://doi.org/10.1007/s00382-017-3682-1>.
- Colman, R., 2003: A comparison of climate feedbacks in general circulation models. *Climate Dyn.*, **20**, 865–873, <https://doi.org/10.1007/s00382-003-0310-z>.
- , and B. J. McAvaney, 1997: A study of general circulation model climate feedbacks determined from perturbed sea surface temperature experiments. *J. Geophys. Res.*, **102**, 19 383–19 402, <https://doi.org/10.1029/97JD00206>.
- Di Lorenzo, E., and N. Mantua, 2016: Multi-year persistence of the 2014/15 North Pacific marine heatwave. *Nat. Climate Change*, **6**, 1042–1047, <https://doi.org/10.1038/nclimate3082>.
- Forster, P., and Coauthors, 2021: The Earth's energy budget, climate feedbacks, and climate sensitivity. *Climate Change 2021: The Physical Science Basis*. V. Masson-Delmotte et al., Eds., Cambridge University Press, 923–1054, <https://doi.org/10.1017/9781009157896.009>.
- Gelaro, R., and Coauthors, 2017: The Modern-Era Retrospective Analysis for Research and Applications, version 2 (MERRA-2). *J. Climate*, **30**, 5419–5454, <https://doi.org/10.1175/JCLI-D-16-0758.1>.
- Hartmann, D. L., and K. Larson, 2002: An important constraint on tropical cloud–climate feedback. *Geophys. Res. Lett.*, **29**, 1951, <https://doi.org/10.1029/2002GL015835>.
- Hu, Y., and Q. Fu, 2007: Observed poleward expansion of the Hadley circulation since 1979. *Atmos. Chem. Phys.*, **7**, 5229–5236, <https://doi.org/10.5194/acp-7-5229-2007>.
- Jakob, C., and G. Tselioudis, 2003: Objective identification of cloud regimes in the tropical western Pacific. *Geophys. Res. Lett.*, **30**, 2082, <https://doi.org/10.1029/2003GL018367>.
- Jin, D., and B. P. Kirtman, 2009: Why the Southern Hemisphere ENSO responses lead ENSO. *J. Geophys. Res.*, **114**, D23101, <https://doi.org/10.1029/2009JD012657>.
- , L. Oreopoulos, D. Lee, J. Tan, and N. Cho, 2021: Cloud–precipitation hybrid regimes and their projection onto IM-ERG precipitation data. *J. Appl. Meteor. Climatol.*, **60**, 733–748, <https://doi.org/10.1175/JAMC-D-20-0253.1>.
- , —, —, —, and K.-M. Kim, 2022: A new organization metric for synoptic scale tropical convective aggregation. *J. Geophys. Res. Atmos.*, **127**, e2022JD036665, <https://doi.org/10.1029/2022JD036665>.
- , D. Kim, S.-W. Son, and L. Oreopoulos, 2023: QBO deepens MJO convection. *Nat. Commun.*, **14**, 4088, <https://doi.org/10.1038/s41467-023-39465-7>.
- Kamae, Y., H. Shiogama, M. Watanabe, T. Ogura, T. Yokohata, and M. Kimoto, 2016: Lower-tropospheric mixing as a constraint on cloud feedback in a multiparameter multiphysics ensemble. *J. Climate*, **29**, 6259–6275, <https://doi.org/10.1175/JCLI-D-16-0042.1>.
- Klein, S. A., and C. Jakob, 1999: Validation and sensitivities of frontal clouds simulated by the ECMWF model. *Mon. Wea. Rev.*, **127**, 2514–2531, [https://doi.org/10.1175/1520-0493\(1999\)127<2514:VASOFC>2.0.CO;2](https://doi.org/10.1175/1520-0493(1999)127<2514:VASOFC>2.0.CO;2).
- Knutson, T., and Coauthors, 2019: Tropical cyclones and climate change assessment: Part I: Detection and attribution. *Bull. Amer. Meteor. Soc.*, **100**, 1987–2007, <https://doi.org/10.1175/BAMS-D-18-0189.1>.
- Koshiro, T., H. Kawai, and A. T. Noda, 2022: Estimated cloud-top entrainment index explains positive low-cloud-cover feedback. *Proc. Natl. Acad. Sci. USA*, **119**, e2200635119, <https://doi.org/10.1073/pnas.2200635119>.
- Loeb, N. G., and Coauthors, 2018: Clouds and the Earth's Radiant Energy System (CERES) Energy Balanced and Filled (EBAF) Top-of-Atmosphere (TOA) edition-4.0 data product. *J. Climate*, **31**, 895–918, <https://doi.org/10.1175/JCLI-D-17-0208.1>.
- , G. C. Johnson, T. J. Thorsen, J. M. Lyman, F. G. Rose, and S. Kato, 2021: Satellite and ocean data reveal marked increase in Earth's heating rate. *Geophys. Res. Lett.*, **48**, e2021GL093047, <https://doi.org/10.1029/2021GL093047>.
- Lu, J., G. A. Vecchi, and T. Reichler, 2007: Expansion of the Hadley cell under global warming. *Geophys. Res. Lett.*, **34**, L06805, <https://doi.org/10.1029/2006GL028443>.
- Mantua, N. J., S. R. Hare, Y. Zhang, J. M. Wallace, and R. C. Francis, 1997: A Pacific interdecadal climate oscillation with impacts on salmon production. *Bull. Amer. Meteor. Soc.*, **78**, 1069–1080, [https://doi.org/10.1175/1520-0477\(1997\)078<1069:APICOW>2.0.CO;2](https://doi.org/10.1175/1520-0477(1997)078<1069:APICOW>2.0.CO;2).
- Meng, L., J. Liu, D. W. Tarasick, W. J. Randel, A. K. Steiner, H. Wilhelmson, L. Wang, and L. Haimberger, 2021:

- Continuous rise of the tropopause in the Northern Hemisphere over 1980–2020. *Sci. Adv.*, **7**, eabi8065, <https://doi.org/10.1126/sciadv.abi8065>.
- Myhre, G., and Coauthors, 2018: Quantifying the importance of rapid adjustments for global precipitation changes. *Geophys. Res. Lett.*, **45**, 11 399–11 405, <https://doi.org/10.1029/2018GL079474>.
- Norris, J. R., R. J. Allen, A. T. Evan, M. D. Zelinka, C. W. O'Dell, and S. A. Klein, 2016: Evidence for climate change in the satellite cloud record. *Nature*, **536**, 72–75, <https://doi.org/10.1038/nature18273>.
- O'Gorman, P. A., R. P. Allan, M. P. Byrne, and M. Previdi, 2012: Energetic constraints on precipitation under climate change. *Surv. Geophys.*, **33**, 585–608, <https://doi.org/10.1007/s10712-011-9159-6>.
- Park, S., and C. B. Leovy, 2004: Marine low-cloud anomalies associated with ENSO. *J. Climate*, **17**, 3448–3469, [https://doi.org/10.1175/1520-0442\(2004\)017<3448:MLAAWE>2.0.CO;2](https://doi.org/10.1175/1520-0442(2004)017<3448:MLAAWE>2.0.CO;2).
- Platnick, S., and Coauthors, 2017: The MODIS cloud optical and microphysical products: Collection 6 updates and examples from Terra and Aqua. *IEEE Trans. Geosci. Remote Sens.*, **55**, 502–525, <https://doi.org/10.1109/TGRS.2016.2610522>.
- , and Coauthors, 2018: MODIS cloud optical properties: User guide for the collection 6/6.1 Level-2 MOD06/MYD06 product and associated Level-3 datasets, version 1.1. 150 pp., https://atmosphere-imager.gsfc.nasa.gov/sites/default/files/ModAtmo/MODISCloudOpticalPropertyUserGuideFinal_v1.1_1.pdf.
- Raghuraman, S. P., D. Paynter, R. Menzel, and V. Ramaswamy, 2023: Forcing, cloud feedbacks, cloud masking, and internal variability in the cloud radiative effect satellite record. *J. Climate*, **36**, 4151–4167, <https://doi.org/10.1175/JCLI-D-22-0555.1>.
- Rayner, N. A., D. E. Parker, E. B. Horton, C. K. Folland, L. V. Alexander, D. P. Rowell, E. C. Kent, and A. Kaplan, 2003: Global analyses of sea surface temperature, sea ice, and night marine air temperature since the late nineteenth century. *J. Geophys. Res.*, **108**, 4407, <https://doi.org/10.1029/2002JD002670>.
- Richardson, M. T., R. J. Roy, and M. D. Lebsock, 2022: Satellites suggest rising tropical high cloud altitude: 2002–2021. *Geophys. Res. Lett.*, **49**, e2022GL098160, <https://doi.org/10.1029/2022GL098160>.
- Rossow, W. B., and R. A. Schiffer, 1991: ISCCP cloud data products. *Bull. Amer. Meteor. Soc.*, **72**, 2–20, [https://doi.org/10.1175/1520-0477\(1991\)072<0002:ICDP>2.0.CO;2](https://doi.org/10.1175/1520-0477(1991)072<0002:ICDP>2.0.CO;2).
- , and —, 1999: Advances in understanding clouds from ISCCP. *Bull. Amer. Meteor. Soc.*, **80**, 2261–2288, [https://doi.org/10.1175/1520-0477\(1999\)080<2261:AIUCFI>2.0.CO;2](https://doi.org/10.1175/1520-0477(1999)080<2261:AIUCFI>2.0.CO;2).
- , G. Tselioudis, A. Polak, and C. Jakob, 2005: Tropical climate described as a distribution of weather states indicated by distinct mesoscale cloud property mixtures. *Geophys. Res. Lett.*, **32**, L21812, <https://doi.org/10.1029/2005GL024584>.
- Santoso, A., M. J. McPhaden, and W. Cai, 2017: The defining characteristics of ENSO extremes and the strong 2015/2016 El Niño. *Rev. Geophys.*, **55**, 1079–1129, <https://doi.org/10.1002/2017RG000560>.
- Smith, C. J., and Coauthors, 2020: Effective radiative forcing and adjustments in CMIP6 models. *Atmos. Chem. Phys.*, **20**, 9591–9618, <https://doi.org/10.5194/acp-20-9591-2020>.
- Soden, B. J., and I. M. Held, 2006: An assessment of climate feedbacks in coupled ocean–atmosphere models. *J. Climate*, **19**, 3354–3360, <https://doi.org/10.1175/JCLI3799.1>.
- , A. J. Broccoli, and R. S. Hemler, 2004: On the use of cloud forcing to estimate cloud feedback. *J. Climate*, **17**, 3661–3665, [https://doi.org/10.1175/1520-0442\(2004\)017<3661:OTUOCF>2.0.CO;2](https://doi.org/10.1175/1520-0442(2004)017<3661:OTUOCF>2.0.CO;2).
- , I. M. Held, R. Colman, K. M. Shell, J. T. Kiehl, and C. A. Shields, 2008: Quantifying climate feedbacks using radiative kernels. *J. Climate*, **21**, 3504–3520, <https://doi.org/10.1175/2007JCLI2110.1>.
- Stevens, B., S. C. Sherwood, S. Bony, and M. J. Webb, 2016: Prospects for narrowing bounds on Earth's equilibrium climate sensitivity. *Earth's Future*, **4**, 512–522, <https://doi.org/10.1002/2016EF000376>.
- Sun, M., D. R. Doelling, N. G. Loeb, R. C. Scott, J. Wilkins, L. T. Nguyen, and P. Mlynzack, 2022: Clouds and the Earth's Radiant Energy System (CERES) FluxByCldTyp edition 4 data product. *J. Atmos. Oceanic Technol.*, **39**, 303–318, <https://doi.org/10.1175/JTECH-D-21-0029.1>.
- Tselioudis, G., W. Rossow, Y. Zhang, and D. Konsta, 2013: Global weather states and their properties from passive and active satellite cloud retrievals. *J. Climate*, **26**, 7734–7746, <https://doi.org/10.1175/JCLI-D-13-00024.1>.
- , —, C. Jakob, J. Remillard, D. Tropic, and Y. Zhang, 2021: Evaluation of clouds, radiation, and precipitation in CMIP6 models using global weather states derived from ISCCP-H cloud property data. *J. Climate*, **34**, 7311–7324, <https://doi.org/10.1175/JCLI-D-21-0076.1>.
- Tseng, Y.-H., R. Ding, and X.-m. Huang, 2017: The warm Blob in the northeast Pacific—The bridge leading to the 2015/16 El Niño. *Environ. Res. Lett.*, **12**, 054019, <https://doi.org/10.1088/1748-9326/aa67c3>.
- Webb, M., C. Senior, S. Bony, and J.-J. Morcrette, 2001: Combining ERBE and ISCCP data to assess clouds in the Hadley Centre, ECMWF and LMD atmospheric climate models. *Climate Dyn.*, **17**, 905–922, <https://doi.org/10.1007/s003820100157>.
- Wetherald, R. T., and S. Manabe, 1988: Cloud feedback processes in a general circulation model. *J. Atmos. Sci.*, **45**, 1397–1416, [https://doi.org/10.1175/1520-0469\(1988\)045<1397:CFPIAG>2.0.CO;2](https://doi.org/10.1175/1520-0469(1988)045<1397:CFPIAG>2.0.CO;2).
- Williams, A. I. L., N. Jeevanjee, and J. Bloch-Johnson, 2023: Circulations, convective thresholds, and the non-linear climate response to tropical SSTs. *Geophys. Res. Lett.*, **50**, e2022GL101499, <https://doi.org/10.1029/2022GL101499>.
- Zelinka, M. D., S. A. Klein, and D. L. Hartmann, 2012a: Computing and partitioning cloud feedbacks using cloud property histograms. Part I: Cloud radiative kernels. *J. Climate*, **25**, 3715–3735, <https://doi.org/10.1175/JCLI-D-11-00248.1>.
- , —, and —, 2012b: Computing and partitioning cloud feedbacks using cloud property histograms. Part II: Attribution to changes in cloud amount, altitude, and optical depth. *J. Climate*, **25**, 3736–3754, <https://doi.org/10.1175/JCLI-D-11-00249.1>.
- , —, K. E. Taylor, T. Andrews, M. J. Webb, J. M. Gregory, and P. M. Forster, 2013: Contributions of different cloud types to feedbacks and rapid adjustments in CMIP5. *J. Climate*, **26**, 5007–5027, <https://doi.org/10.1175/JCLI-D-12-00555.1>.
- , C. Zhou, and S. A. Klein, 2016: Insights from a refined decomposition of cloud feedbacks. *Geophys. Res. Lett.*, **43**, 9259–9269, <https://doi.org/10.1002/2016GL069917>.
- , T. A. Myers, D. T. McCoy, S. Po-Chedley, P. M. Caldwell, P. Ceppi, S. A. Klein, and K. E. Taylor, 2020: Causes of higher climate sensitivity in CMIP6 models. *Geophys. Res. Lett.*, **46**, e2019GL085782, <https://doi.org/10.1029/2019GL085782>.
- , I. Tan, L. Oreopoulos, and G. Tselioudis, 2023: Detailing cloud property feedbacks with a regime-based decomposition. *Climate Dyn.*, **60**, 2983–3003, <https://doi.org/10.1007/s00382-022-06488-7>.

- Zhang, B., R. J. Kramer, and B. J. Soden, 2019: Radiative feedbacks associated with the Madden–Julian oscillation. *J. Climate*, **32**, 7055–7065, <https://doi.org/10.1175/JCLI-D-19-0144.1>.
- Zhang, M. H., J. J. Hack, J. T. Kiehl, and R. D. Cess, 1994: Diagnostic study of climate feedback processes in atmospheric general circulation models. *J. Geophys. Res.*, **99**, 5525–5537, <https://doi.org/10.1029/93JD03523>.
- Zhou, C., M. D. Zelinka, A. E. Dessler, and S. A. Klein, 2015: The relationship between interannual and long-term cloud feedbacks. *Geophys. Res. Lett.*, **42**, 10 463–10 469, <https://doi.org/10.1002/2015GL066698>.
- , —, and S. A. Klein, 2016: Impact of decadal cloud variations on the Earth’s energy budget. *Nat. Geosci.*, **9**, 871–874, <https://doi.org/10.1038/ngeo2828>.
- Zhu, P., J. J. Hack, J. T. Kiehl, and C. S. Bretherton, 2007: Climate sensitivity of tropical and subtropical marine low cloud amount to ENSO and global warming due to doubled CO₂. *J. Geophys. Res.*, **112**, D17108, <https://doi.org/10.1029/2006JD008174>.